Proceedings of the Twenty-eighth (2018) International Ocean and Polar Engineering Conference
Sapporo, Japan, June 10-15, 2018

ISBN 978-1-880653-87-6; ISSN 1098-6189

www.isope.org

CFD Investigation of Flow Interactions of Four Fixed Columns with Free Ends in Square Configuration

*Jiawei He, Weiwen Zhao, Decheng Wan**
State Key Laboratory of Ocean Engineering, School of Naval Architecture, Ocean and Civil Engineering, Shanghai Jiao Tong University, Collaborative Innovation Center for Advanced Ship and Deep-Sea Exploration, Shanghai, China
*Corresponding author

ABSTRACT

Numerical simulations are carried out by the in-house naoe-FOAM-SJTU solver based on the OpenFOAM framework. Delayed Detached-Eddy Simulation (DDES) method based on the Shear-Stress Transport (SST) model is used to simulate the large separated flow in high Reynolds numbers, *Re* = 50,000. CFD simulations are carried out for three different column geometries, namely circular, square and diamond. To further illustrate the vortex shedding characteristics of interaction between wakes in the array of cylinders, the results of mean drag and RMS lift force coefficients are analyzed for each column. The mean drag and RMS lift force coefficients of each column are in generally good agreement with experimental results. The instantaneous vortex shedding structures of three different column geometries are also presented. A tip vortex is observed around the free end of upstream columns, while it is not obvious around the free end of downstream columns. Results show that the effect of column section geometries to the mean drag force coefficients and wake flows of upstream columns is very significant.

KEY WORDS: Flow around fixed columns, SST-DDES, CFD, naoe-FOAM-SJTU solver.

INTRODUCTION

A floating body in a flow experiences periodic motion and this motion is called vortex-induced motion (VIM). VIM is induced by vortex associated with the separation of boundary layer at the body surface. The analysis of vortex-induced motions (VIM) is of great importance during the design process of a floating offshore platform since the unsteady VIM phenomenon has significant influences on the fatigue life of mooring and riser systems. Most of the semi-submersibles and TLP offshore platforms consist of four columns. Investigating the flow interaction between each column can reveal some physics behind the VIM. What's more, the flow field around the multi-column platforms is more complex than the single cylindrical structures due to the mutual interfere between cylinders which generates complex wake-structure interaction process in vortex-shedding. Hence, a pre-research work is conducted here to lay a foundation for the future study of semi-submersibles offshore platform's VIM phenomenon.

Flow past infinite, fully submerged cylinders is well understood, due to ample experimental and numerical studies. (Singh and Mittal, 2005)has given a comprehensive description of the flow phenomena at different Reynolds numbers (Re). Flow over the circular cylinder's free end cause the local flow field and the cylinder's wake to become strongly three-dimensional, the flow over a wall-mounted finite-length cylinder is drastically different from that behind a two-dimensional cylinder(Sumner et al., 2004). The main flow features schematic of the free-end flow field for finite-height circular cylinder is showing in Fig1.

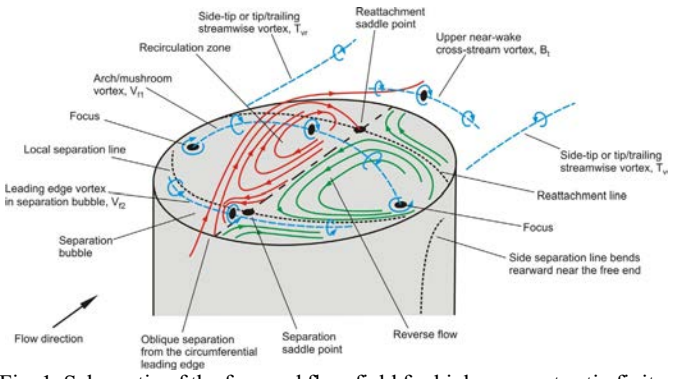

Fig. 1. Schematic of the free-end flow field for higher-aspect-ratio finite-height circular cylinder showing the main flow features(Rostamy et al., 2014).

Krajnović (2011), have extensively addressed the influence and structure of the flow above the free-end surface, how this flow field relates to what is happening in the near-wake region, and how this local flow field is influenced by various parameters such as Reynolds number, aspect ratio, and the boundary layer thickness(Krajnović, 2011). Recent PIV experiments by Rostamy et al. (2012) provided results for the mean recirculation zone in the vertical symmetry plane for finite circular cylinders with different aspect ratio at Re=4.2×10^4. Rostamy et al. (2012) did not observe significant differences to the mean recirculation zone

with different aspect ratio (Rostamy et al., 2012). Goncalves et al. (2015) have shown the existence of a critical aspect ratio below which the cylinder has a distinct wake structure, he also pointed out that a decrease in drag force coefficients with decreasing aspect ratio, as well as a decrease in Strouhal number with decreasing aspect ratio (Goncalves et al., 2015). Zhao et al. (2016) presents a numerical study of flow over a circular cylinder at high Reynolds number using detached-eddy simulation (DES) (Zhao et al., 2016).

Most of the researches are focused on flow around an isolated circular cylinder or two cylinders, as pointed by Bourgeois et al., Krajnović and Wang et al. (Bourgeois et al., 2011; Krajnović, 2011; Wang et al., 2012). However, few investigations are performed to reveal the flow dynamics of a four-square-arranged configuration, which is essential for various marine structures as a fundamental arrangement. Islam et al(2009) present a numerical study of a uniform flow past four cylinders in an in-line rectangular configuration using the lattice Boltzmann method. He also found that the Strouhal number for all four cylinders are almost equal for all chosen spacing ratios even there are more than one dominant frequency for small spacing ratios(Islam et al., 2009). Anagnostopoulos et al study the computational simulation of viscous oscillatory flow past four circular cylinders is conducted, using the finite-element technique(Anagnostopoulos et al., 2011). Zhao and Cheng numerical simulation of vortex-induced vibration of four circular cylinders in a square configuration. The numerical results show that the approaching angle has significant effects on the response of the four-cylinder system. The hydrodynamic forces, especially those on the two downstream cylinders, are very irregular(Zhao and Cheng, 2012). Gonçalves et al. study the flow around the cylinders and the interference between the wakes due to the positioning of the cylinders. He found that when spacing ratio (S/L) values decrease below S/L = 1.70, only a wide wake is found attached to the doublet of cylinders, similar to the behavior of a single cylinder. For values of spacing ratio above S/L = 4.00, the wake is well established in each of the four cylinders (Goncalves et al., 2016).

In general, the investigation of unsteady viscous flow past a single or array of columns is of great interest for both the fundamental turbulence research and engineering applications such as offshore platforms (semi-submersible). The main objective of this paper is to investigate the flow interactions between multi-columns based on CFD methods.

TURBULENCE MODELING

In the present study, the turbulent model is using the Shear Stress Transport (SST) based Delay Detached eddy simulation (DDES), which provides the accuracy of LES for highly separated flow regions and computational efficiency of RANS in the near-wall region, making it applicable to the simulation of VIM. In the SST-DDES turbulence model, the computed turbulent length scale is defined as:

$$l_{DDES} = l_{RANS} - f_d max(0, l_{RANS} - C_{DES}\Delta) \quad (1)$$

Where, $l_{RANS} = \frac{\sqrt{k}}{\beta^* \omega}$ is the RANS computed turbulent length scale; $\Delta = \sqrt[3]{V}$ is size of sub-grid;

$$C_{DES} = (1 - F_1){C_{DES}}^{k-\varepsilon} + F_1 {C_{DES}}^{k-\omega} \quad (2)$$

$$f_d = 1 - \tanh[(C_{d1} r_d)^{C_{d2}}] \quad (3)$$

$$r_d = \frac{v_t + v}{\kappa^2 {d_w}^2 \sqrt{0.5(S^2 + \Omega^2)}} 1 - \tanh[(C_{d1} r_d)^{C_{d2}}] \quad (4)$$

v_t, v are the eddy and molecular viscosities respectively, κ = 0.41 is the von-Kaman constant. C_{DES} is the DES constant which is 0.61, F_S can be F_1 or F_2, and F_2 is used in the paper of Zhao et al (2016). The suitability of the present SST-DDES model has been clarified by Zhao et al (2016) for solving flow past two circular cylinders in tandem. More about the SST-DDES model can also be seeing in Zhao's paper(Wei-wen and De-cheng, 2016).

NUMERICAL TREATMENT

Domain and Grids

The multi-column platforms present four circular, square or diamond columns, which increases the differences as compared to the single circular cylinder. The wake interference is different for different section geometries. In present study,One parameter was investigated: three different section geometries (cylinder, square and diamond). Force measurements are conducted in each column separately. Fig. 2 shows the sketch of the array with different column section geometries. Hence, the cross section used in the numerical computations corresponds exactly to the one used in the experiments (Gonçalves et al., 2017). The velocities of uniform current, in m/s, is U_0=0.2, which corresponds to a Reynolds number range of Re=50,000. And the current incidence angle is equal to 0 degree in present study. The case of different current velocities for each combination of column section geometry and current incidence angle will be performed in my future study work.

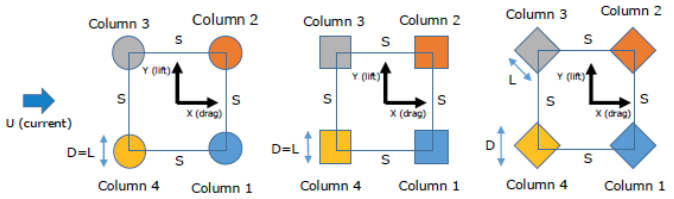

Fig. 2 - Sketch of the array with different column section geometries, Spacing ratio S/L=3 for the array of four columns and 0-degree incidence. Picture from Goncalves et al(Gonçalves et al., 2017)

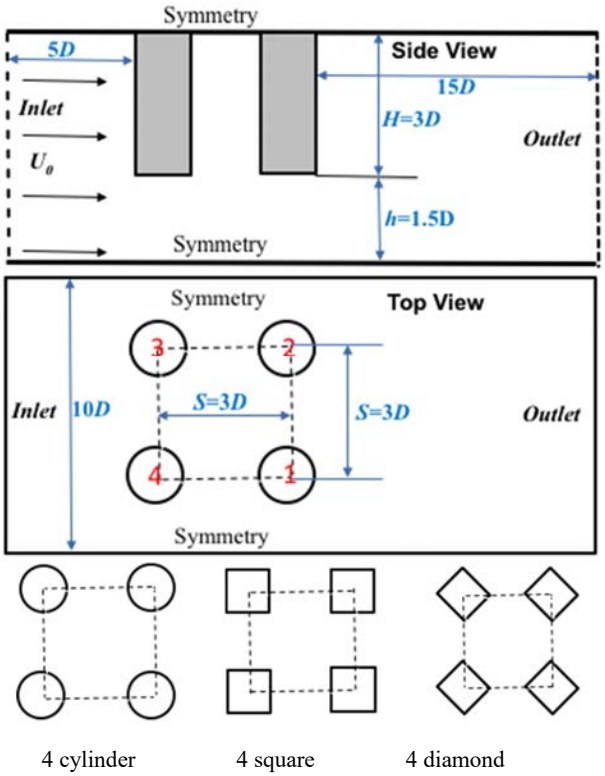

Fig. 3. Sketch of the computational domain and boundary condition

The calculation domain shows in Fig. 3. The domain of the background grid extends to $-5D \leq x \leq 15D$, $-5D \leq y \leq 5D$ and $-4.5D \leq z \leq 0$, where D is characteristic length. The inlet boundary is defined as uniform incoming flow(U_0)with velocity equal to 0.2m/s, i.e. $U_0 = 0.2$m/s. At the outlet boundary, the pressure gradient is set equal to 0. The boundary condition on the columns surface is set to no-slip. The rest of the boundaries is defined as symmetry boundary. Table 1 shows the details of the mesh used with 6 different case conditions in this paper. The computation durations of each test condition are the same for 120 seconds, with a time step for Δt =0.005s.

Table 1. Flow past four fixed columns with different section geometries in square configuration at *Re*=50000: details of the mesh used with 6 different case conditions.

Column geometry	Column Number	F_r	total number of cells (million)	Spacing ratio S/L	Incidence angle
circular	4	0.13	4.24	3	0º
square	4	0.13	3.68	3	0º
diamond	4	0.13	4.00	3	0º
circular	1	0.13	2.59	-	0º
square	1	0.13	2.19	-	0º
diamond	1	0.13	2.21	-	0º

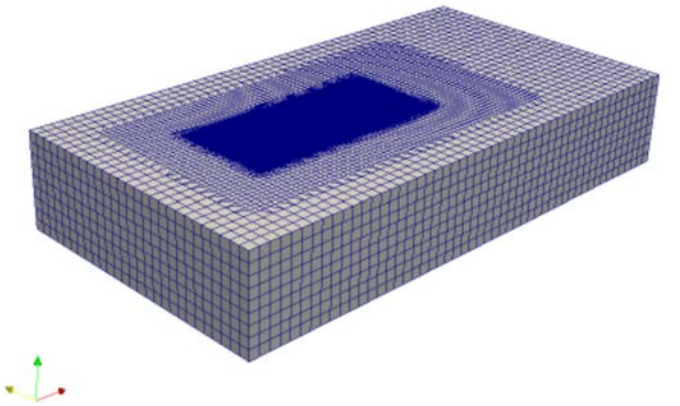

(a) Overhead view of the numerical mesh grids.

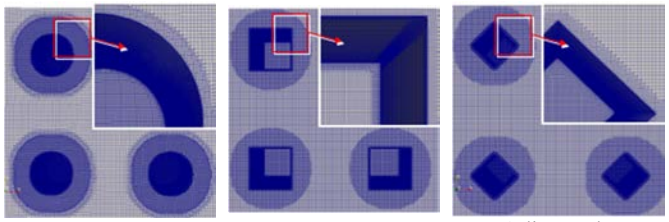

4 cylinder 4 square 4 diamond

(b) View of the numerical mesh grids from the top. Increased cell refinement is located around the 4 columns

Fig. 4. Global and local mesh grids (a) Overhead view of the numerical grids (b) View of the numerical grids from the top. Increased cell refinement is located around the 4 columns

The resulting grids (details of the grids in Fig. 3 and Table1) yielding a maximum of 4.24 Million grid cells for 4 cylinders case. A very fine grid near the column surface and free-end region. The first layer length is 0.00034D, corresponding to approximately y^+=1. Global and local mesh grids is shown in Fig. 4.

Discretization Format

As the Froude numbers were small, the free surface effect can be ignored(Liu et al., 2017). correspondingly, the free surface was treated as a symmetric boundary. Without the free surface, thus that the simulations in this work can be performed using the single-phase incompressible Navier-Stokes solver pimpleFoam. The incompressible finite volume solver naoe-FOAM-SJTU is used for all the computations and the Detached-Eddy Simulations (DES) is selected for turbulence closure. The naoe-FOAM-SJTU solver is a powerful CFD solver based on the open source CFD package, OpenFOAM. It has been proven that naoe-FOAM-SJTU solver is applicable for solving various kinds of nonlinear ship and ocean engineering problems (Zhou et al., 2013), (Shen and Wan, 2014), (Cao and Wan, 2015). The time discretization is done using second order implicit Euler scheme. A second order Gauss integration is used for spatial gradient calculations. The convection operator is discretized using a total variation diminishing (TVD) scheme. The merged PISO-SIMPLE (PIMPLE) algorithm is used for solving the coupled pressure–velocity equations.

RESULTS

The Drag Force Coefficient

The drag non-dimensional forces coefficient is given by:

$$C_d(t) = \frac{2F_x(t)}{\rho HDU^2} \quad (5)$$

Where $F_x(t)$ is the force in the in-line direction; U is the velocity of flow; ρ is the density of water; D, in this case, is the projected length (or characteristic diameter).

Table 2 Mean drag coefficients from present numerical calculations and experiments by Gonçalves et. al (2017)。

Column geometry	Time average drag force coefficient $C_{d,Mean}$	Col 1	Col 2	Col 3	Col 4	Single column
Cylinder	Experiment by Gonçalves et. al	0.37	0.38	0.75	0.76	0.86
	Present CFD	0.413	0.421	0.796	0.793	0.893
	Difference (%)	11.62	10.78	4.60	4.34	3.83
Square	Experiment by Gonçalves et. al	0.13	0.13	1.38	1.39	1.35
	Present CFD	0.231	0.194	1.369	1.378	1.282
	Difference (%)	77.6	49.2	0.79	0.86	5.03
Diamond	Experiment by Gonçalves et. al	0.22	0.22	1.08	1.06	0.97
	Present CFD	0.305	0.372	1.055	1.036	1.018
	Difference (%)	38.6	69.1	2.31	2.26	4.95

*The upstream columns are Col3 and Col4 in table, The downstream columns are Col1 and Col2 in this table and paper.

Table 2 and Fig.5 show the mean drag coefficients from present numerical calculations and experiments by Gonçalves et. al (2017). The calculated mean drag coefficient shows that the computed results of upstream cylinders (Col3 and Col4) and those of downstream cylinders (Col1 and Col2) are almost equal. From the Table 2, we find that the time average drag force coefficient C_d is vary drastically with the changes of section geometries. Firstly, for case of upstream cylinders (Col3 and Col4), the value of $C_{d,Mean}$ is relatively lower comparing with those of

other two section geometries (square and diamond). For downstream cylinder (Col1 and Col2), $C_{d,Mean}$ is different case and the value is higher at $C_{d,Mean} \approx 0.38$. Secondly, for case of upstream squares, the value of $C_{d,Mean}$ is highest around different column geometries. Lastly, it is must be pointed out that the value of $C_{d,Mean}$ in cases of single column are nearly equal to the upstream columns of multicolumn cases. The maximum values of $C_{d,Mean}$ with present CFD considering each column were: 0.79 for the circular case and 1.38 for the square case, or for diamond is 1.04. The mean drag force coefficients revealed that the columns not affected by the disturbed wake followed the single column behavior (columns number 3 and 4 for 0-degree incidence). The columns directly affected by the disturbed wake presented lower values of $C_{d,Mean}$.

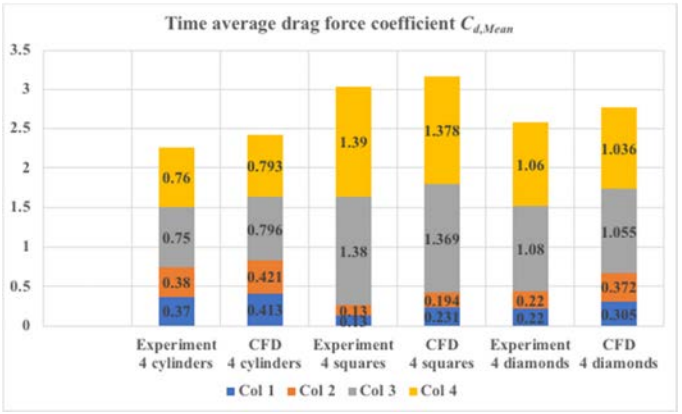

Fig.5. Comparison of mean drag contribution of four columns for different section geometries between columns

Fig. 6 ~Fig.8 present the time history of drag force coefficient results for the circular, the square and the diamond column section cases, respectively. As can be seen from Fig. 6~ and Fig.8, the drag coefficient of upstream columns is fluctuating at very small amplitude. With the evolution of time, while the drag coefficient of downstream columns is still fluctuating drastically. That implies the upstream cylinder at this mode is under a nearly constant force.

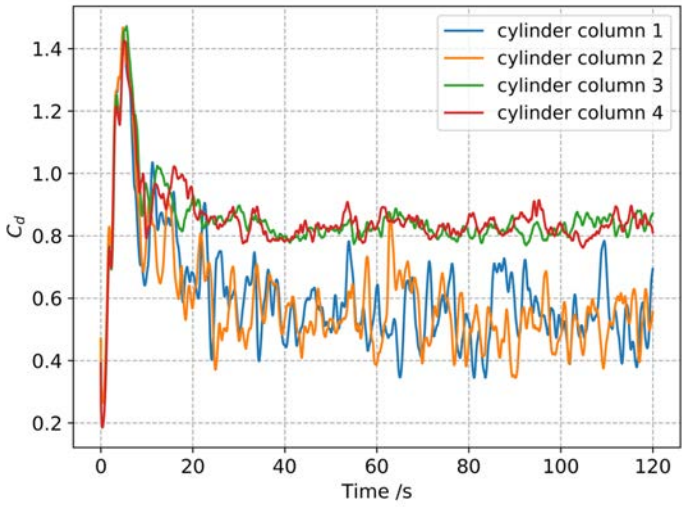

Fig. 6. Time history of drag coefficients of four cylinders

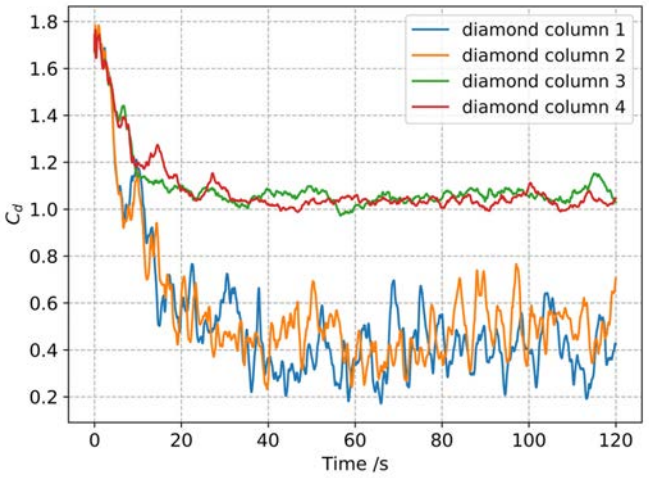

Fig. 7. Time history of drag coefficients of four diamonds

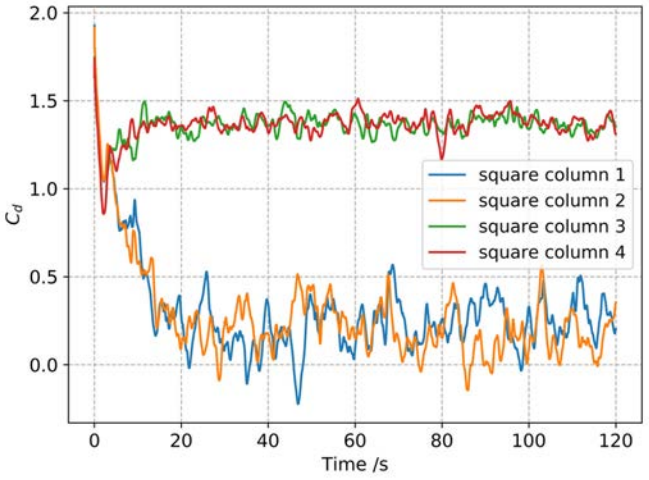

Fig. 8. Time history of drag coefficients of four squares

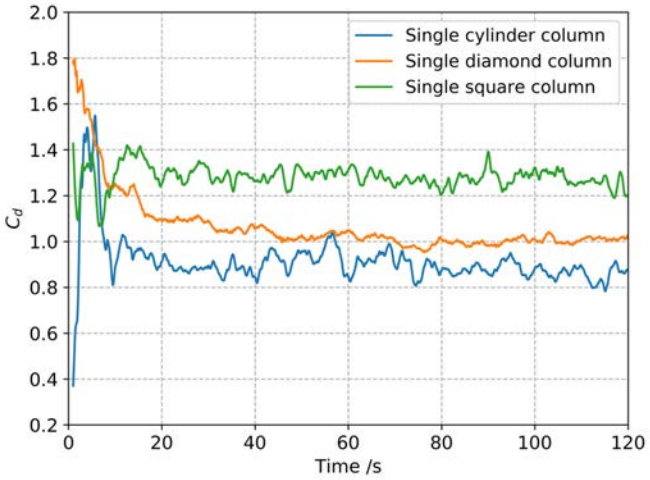

Fig. 9. Time history of drag coefficients of single column with different section geometries

The Fig. 9 shows the time history of drag coefficients of single columns with different section geometries. With the evolution of time, the relationship of drag coefficients between different section geometries is $C_{d,square} > C_{d,diamond} > C_{d,cylinder}$.

Root Mean Square (RMS) Drag Coefficient $C_{d,RMS}$

Table 3 RMS of drag coefficient for different section geometry column case

Column geometry	Root mean square (RMS) drag coefficient $C_{d,RMS}$	Col 1	Col 2	Col 3	Col 4	Single column
Cylinder	Experiment by Gonçalves et. al	0.08	0.08	0.05	0.05	0.042
	Present CFD	0.087	0.086	0.037	0.036	0.051
	Difference (%)	8.75	7.50	26.0	28.0	21.4
Square	Experiment by Gonçalves et. al	0.15	0.15	0.062	0.065	0.05
	Present CFD	0.130	0.129	0.054	0.059	0.055
	Difference (%)	13.3	14.0	11.7	9.23	10.0
Diamond	Experiment by Gonçalves et. al	0.12	0.11	0.042	0.043	0.038
	Present CFD	0.123	0.101	0.038	0.036	0.042
	Difference (%)	2.5	9.09	9.52	16.2	10.5

The RMS of drag coefficient $C_{d,RMS}$ for different section geometry column case in Table 3. The results are shown for each column separately and in contrast to single column case, and then compared with the experimental results by Gonçalves et. al (2017). The maximum values of RMS drag coefficient $C_{d,RMS}$ considering each column were: 0.15 for the 4 squares case (almost triple the value for the single square column case).

The Lift Force Coefficient

The lift non-dimensional forces coefficient is given by:

$$C_l(t) = \frac{2F_y(t)}{\rho HDU^2} \tag{6}$$

Where $F_y(t)$ is the force in the transverse direction; U is the velocity of flow; ρ is the density of water; D, in this case, is the projected length (or characteristic diameter).

Fig. 10~ Fig.12 present the time history of lift force coefficient results for the circular, the square and the diamond column section cases, respectively. The results show that the vortex shedding becomes irregular, and the frequencies of the lift coefficients are not periodic. As can be seen from Fig. 6~Fig.8, the drag coefficient of upstream columns is fluctuating at very small amplitude. With the evolution of time, while the drag coefficient of downstream columns is still fluctuating drastically. For the downstream cylinder, both the drag and lift coefficients are fluctuate, however, the amplitude of lift coefficient is much bigger than drag coefficient.

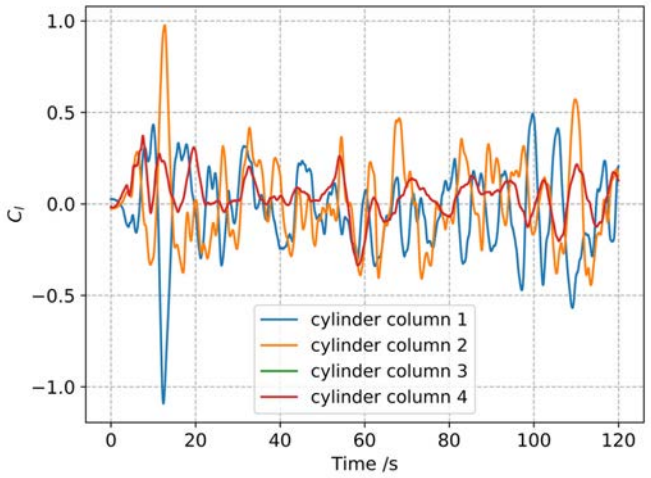

Fig. 10. Time history of lift coefficients of four cylinders

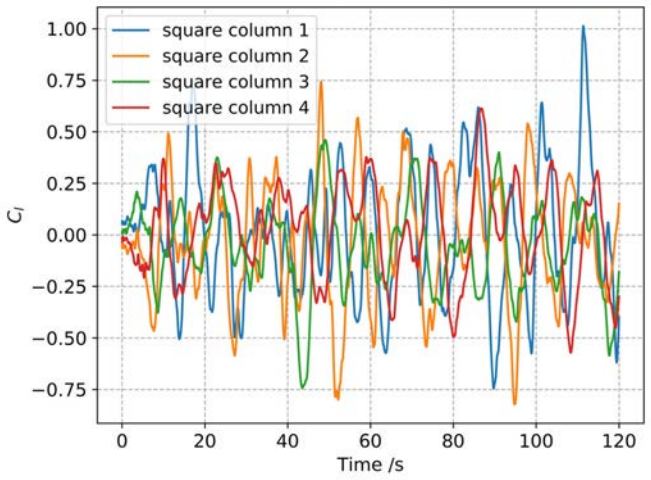

Fig. 11. Time history of lift coefficients of four squares

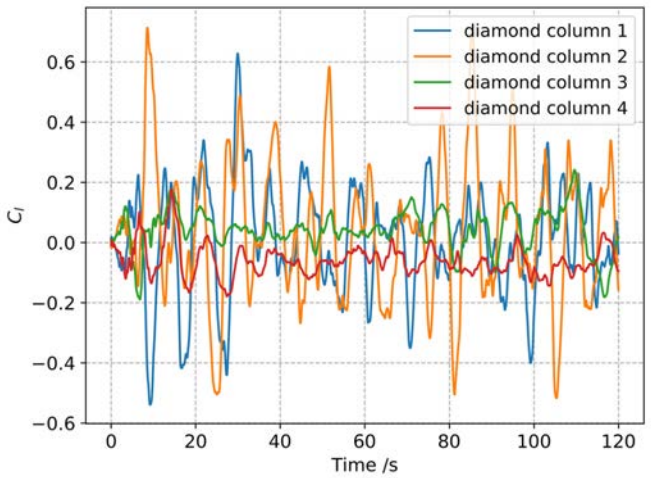

Fig. 12. Time history of lift coefficients of four diamonds

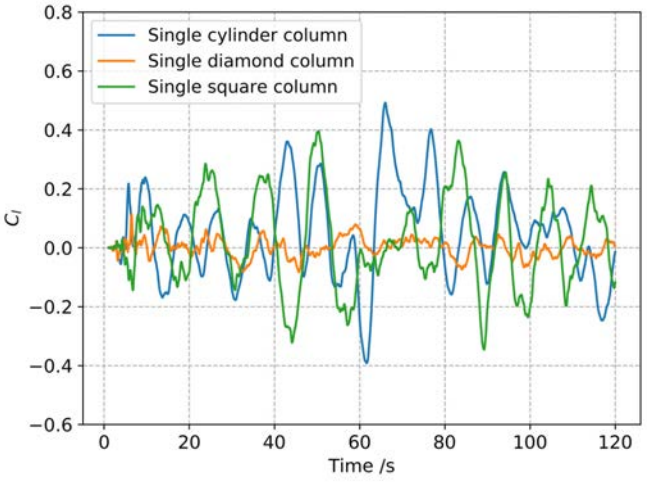

Fig. 13. Time history of lift coefficients of single column with different section geometries

The Fig. 13 shows the time history of lift coefficients of single columns with different section geometries. With the evolution of time, the lift coefficient is still fluctuating drastically. However, the amplitude of fluctuation is the single cylinder larger than single square, and then the single diamond is minimum. And it must be pointed out the amplitude of lift coefficient fluctuation is much bigger than drag coefficient.

Root Mean Square (RMS) Lift Coefficient $C_{l,RMS}$

Table 4 RMS of lift coefficient $C_{l,RMS}$ for different section geometry column case

Column geometry	Root mean square (RMS) lift coefficient $C_{l,RMS}$	Col 1	Col 2	Col 3	Col 4	Single column
Cylinder	Experiment by Gonçalves et. al	0.16	0.15	0.13	0.14	0.10
	Present CFD	0.18	0.18	0.10	0.12	0.12
	Difference (%)	12.5	20.0	23.1	14.3	20.0
Square	Experiment by Gonçalves et. al	0.30	0.27	0.15	0.15	0.11
	Present CFD	0.32	0.29	0.18	0.19	0.13
	Difference (%)	6.67	7.40	20.0	26.7	18.2
Diamond	Experiment by Gonçalves et. al	0.14	0.14	0.05	0.05	0.04
	Present CFD	0.17	0.18	0.052	0.054	0.037
	Difference (%)	21.4	28.6	4.00	8.00	7.50

The RMS of lift coefficient $C_{l,RMS}$for different section geometry column case in Table 4. The results are shown for each column separately and in contrast to single column case. As pointed out by Gonçalves et al(2017), the total RMS lift coefficient results are very important for VIM features (Gonçalves et al., 2017). The results of lift force coefficient are important because the lift force is responsible for promoting large transverse amplitudes of VIM when the system is free to oscillate in the horizontal plane. The maximum values for the cylinder cases is $C_{l,RMS} \approx 0.18$;The maximum values for the square cases is $C_{l,RMS} \approx 0.32$; The maximum values for the diamond cases is $C_{l,RMS} \approx 0.18$.

Instantaneous Vortex Structure

Fig. 14 shows the instantaneous isosurface of vortex structures Q=5, dye visualization with non-dimensioned velocity magnitude. The definition of Q is given by:

$$Q = \frac{1}{2}(|\Omega|^2 - |S|^2) \tag{7}$$

where S is invariant measure of the strain rate tensor, define as $S = \sqrt{2S_{ij}S_{ij}}$, and $S_{ij} = \frac{1}{2}\left(\frac{\partial u_i}{\partial x_j} + \frac{\partial u_j}{\partial x_j}\right)$, Ω is invariant measure of vorticity tensor.

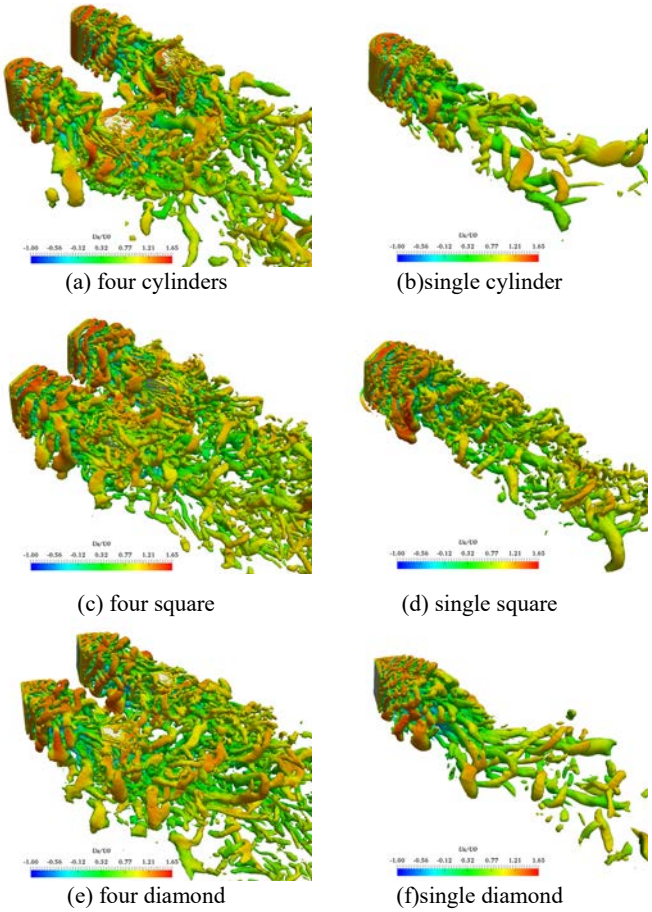

(a) four cylinders (b)single cylinder (c) four square (d) single square (e) four diamond (f)single diamond

Fig. 14. Instantaneous isosurface of vorticity Q=5, dye visualization with non-dimensioned velocity magnitude. (a) four cylinder;(b) single cylinder; (c) four square;(d) single square; (e) four diamond; (d) single diamond.

As shown in Fig. 14, the irregular vortex shedding are visible and the small turbulence structures is showing the fine details with strong 3D effect, which proves our naoe-FOAM-SJTU solver and the SST-DDES method are efficient. The separated flow coming from the free end interacts with the separated flow along the columns and delays the separation. The downstream columns (Col1 and Col2) are mostly located in the wake of upstream columns (Col3 and Col4). As a result, the free shear layers generated from outside of upstream columns reattach onto downstream columns. Immersed in the wake of the upstream columns, the downstream columns always have a lower drag force.

Contours of Vorticity

Fig. 15 is the contours of vorticity Z in the horizontal plane (X-Y plane). In this figure, the wake interferences appeared to be large when the fluctuation of drag force coefficients shows to be large, presented in Fig.

6, Fig. 7, Fig. 8. It is meaning that larger wake interference implies higher values of drag fluctuation.

Fig. 16. is the contours of vorticity magnitude at the central plane(X-Z plane). A tip vortex is observed around the free end of upstream columns; while it is not obvious around the free end of downstream columns. This is due to the vortex shed from the upstream columns changes the downstream region vortex shedding. The vortex detached from the upstream columns directly hit on the downstream columns. This can also be observed from the vorticity contour in Fig. 15.

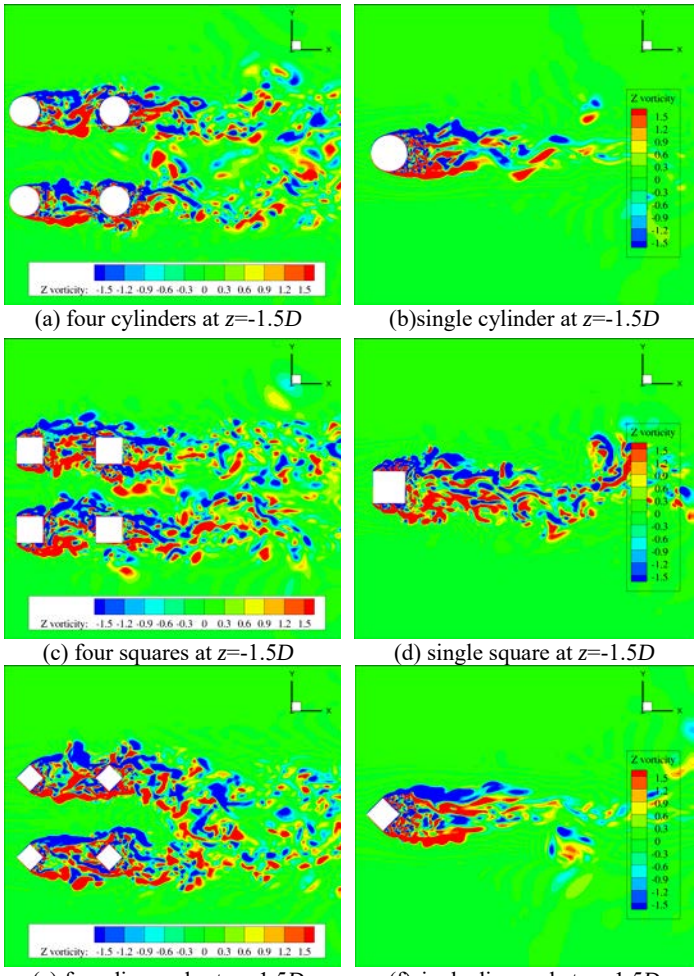

(a) four cylinders at z=-1.5D (b)single cylinder at z=-1.5D

(c) four squares at z=-1.5D (d) single square at z=-1.5D

(e) four diamonds at z=-1.5D (f)single diamond at z=-1.5D

Fig. 15. Contours of vorticity Z in the horizontal plane (a) four cylinder;(b) single cylinder; (c) four square;(d) single square; (e) four diamond; (d) single diamond.

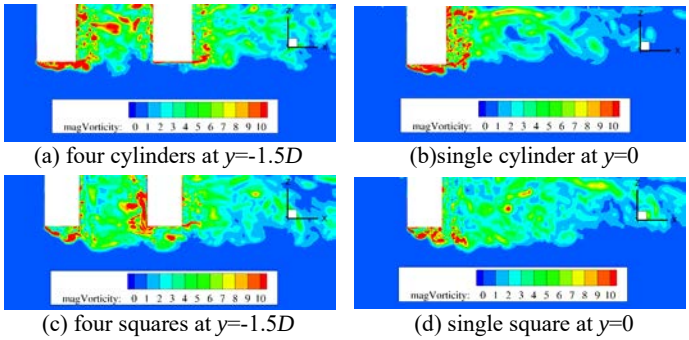

(a) four cylinders at y=-1.5D (b)single cylinder at y=0

(c) four squares at y=-1.5D (d) single square at y=0

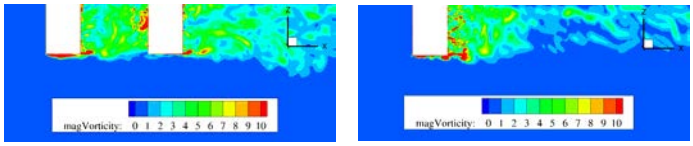

(e) four diamonds at y=-1.5D (f)single diamond at y=0

Fig. 16. Contours of vorticity magnitude at the central plane of columns (a) four cylinder;(b) single cylinder; (c) four square;(d) single square; (e) four diamond; (d) single diamond.

CONCLUSIONS

The flow past four rectangular columns in square configuration has been numerically studied in present work. The numerical predictions show a good agreement with the experiment results in drag force coefficient. The flow characteristics around downstream have been strongly affected by vortex shedding from upstream columns. The downstream columns (Col1 and Col2) are mostly located in the wake of upstream columns (Col3 and Col4). As a result, the free shear layers generated from outside of upstream columns reattach onto downstream columns. Immersed in the wake of the upstream columns, the downstream columns always have a lower drag force. The value of $C_{d,Mean}$ in cases of single column are nearly equal to the upstream columns of multicolumn cases. What's more, a tip vortex is observed around the free end of upstream columns; while it is not obvious around the free end of downstream columns. This study shows the naoe-FOAM-SJTU solver is sufficiently applicable for the simulation of flow around multiple cylindrical structures such as Semi-Submersible and Tension-Leg Platform columns. The case of different current velocities for each combination of column section geometry and current incidence angle will be performed in my future study work. And the expansion to a moored multicolumn is necessary to analyze the effect of end cell and free surface on VIM. This is also left to our future work.

ACKNOWLEDGEMENTS

This work is supported by the National Natural Science Foundation of China (51490675, 11432009, 51579145), Chang Jiang Scholars Program (T2014099), Shanghai Excellent Academic Leaders Program (17XD1402300), Program for Professor of Special Appointment (Eastern Scholar) at Shanghai Institutions of Higher Learning (2013022), Innovative Special Project of Numerical Tank of Ministry of Industry and Information Technology of China (2016-23/09) and Lloyd's Register Foundation for doctoral student, to which the authors are most grateful.

REFERENCES

Anagnostopoulos, P, Dikarou, C, and Seitanis, SA (2011). "Numerical Study of Oscillatory Flow Past Four Cylinders in Square Arrangement for Pitch Ratio Equal to 4," *Vol 7 CFD VIV; Offshore Geotech*, ASME, 457–466.

Bourgeois, JA, Sattari, P, and Martinuzzi, RJ (2011). "Alternating half-loop shedding in the turbulent wake of a finite surface-mounted square cylinder with a thin boundary layer," *Phys Fluids*, 23(9), 095101–095115.

Cao, H, and Wan, D (2015). "Development of Multidirectional Nonlinear Numerical Wave Tank by Naoe-FOAM-SJTU Solver," *J Adv Res Ocean Eng*, 1(1), 14–24.

Goncalves, RT, Franzini, GR, Rosetti, GF, Meneghini, JR, and Fujarra, ALC (2015). "Flow around circular cylinders with very low aspect ratio," *J Fluids Struct*, 54, 122–141.

Goncalves, RT, Hirabayashi, S, and Suzuki, H (2016). "Experimental study on flow around an array of four circular cylinders," *2016 Techno-Ocean*, IEEE, 660–667.

Gonçalves, RT, Hirabayashi, S, and Suzuki, H (2017). "Experimental Study on Flow Around an Array of Four Cylinders With Different Section Geometries," *Vol 2 Prof Carl Martin Larsen Dr Owen Oakley Honor Symp CFD VIV*, ASME, V002T08A018.

Islam, SU, Zhou, CY, and Ahmad, F (2009). "Numerical Simulations of Cross-Flow around Four Square Cylinders in an In-Line Rectangular Configuration," *Int J Mech Mechatronics Eng*, 3(9), 780–789.

Krajnović, S (2011). "Flow around a tall finite cylinder explored by large eddy simulation," *J Fluid Mech*, 676(2011), 294–317.

Liu, M, Xiao, L, Yang, J, Tian, X, Liu, M, Xiao, L, Yang, J, and Tian, X (2017). "Parametric study on the vortex-induced motions of semi-submersibles : Effect of rounded ratios of the column and pontoon Parametric study on the vortex-induced motions of semi-submersibles : Effect of rounded ratios of the column and pontoon," *Phys Fluids*, 29(5), 055101–055119.

Rostamy, N, Sumner, D, Bergstrom, DJ, and Bugg, JD (2012). "Local flow field of a surface-mounted finite circular cylinder," *J Fluids Struct*,.

Rostamy, N, Sumner, D, Bergstrom, DJ, and Bugg, JD (2014). "Flow above the free end of a surface-mounted finite-height cylinder," *Lect Notes Mech Eng*, 8, 167–172.

Shen, Z, and Wan, DC (2014). "Computation of Steady Viscous Flows around Ship with Free Surface by Overset Grids Techniques in OpenFOAM," 3, 832–838.

Singh, SP, and Mittal, S (2005). "Flow past a cylinder: shear layer instability and drag crisis," *Int J Numer Methods Fluids*, 47(1), 75–98.

Sumner, D, Heseltine, JL, and Dansereau, OJP (2004). "Wake structure of a finite circular cylinder of small aspect ratio," *Exp Fluids*, 37(5), 720–730.

Wang, HF, Zhou, Y, and Mi, J (2012). "Effects of aspect ratio on the drag of a wall-mounted finite-length cylinder in subcritical and critical regimes," *Exp Fluids*, 53(2), 423–436.

Zhao, W, Wan, DC, (2016). "Detached-Eddy Simulation of Flow Past Tandem Cylinders," *Appl Math Mech*, 37(12), 1272–1281.

Zhao, M, and Cheng, L (2012). "Numerical simulation of vortex-induced vibration of four circular cylinders in a square configuration," *J Fluids Struct*, 31, 125–140.

Zhao, W, Wan, DC, and Sun, R (2016). "Detached-Eddy Simulation of Flows over a Circular Cylinder at High Reynolds Number," *Proc Twenty-Sixth Int Ocean Polar Eng Conf*, 96(10–11), 1528–1536.

Zhou, H, Cao, H, and Wan, DC (2013). "Numerical predictions of wave impacts on the supporting structures of shanghai donghai-bridge offshore wind turbines," *Proc Int Offshore Polar Eng Conf*, 9, 216–224.